Thermally Controlled, Patterned Graphene Transfer Printing for Transparent and Wearable Electronic/Optoelectronic System

Moon Kee Choi, Inhyuk Park, Dong Chan Kim, Eehyung Joh, Ok Kyu Park, Jaemin Kim, Myungbin Kim, Changsoon Choi, Jiwoong Yang, Kyoung Won Cho, Jae-Ho Hwang, Jwa-Min Nam, Taeghwan Hyeon, Ji Hoon Kim, and Dae-Hyeong Kim**

Graphene has been highlighted as a platform material in transparent electronics and optoelectronics, including flexible and stretchable ones, due to its unique properties such as optical transparency, mechanical softness, ultrathin thickness, and high carrier mobility. Despite huge research efforts for graphene-based electronic/optoelectronic devices, there are remaining challenges in terms of their seamless integration, such as the high-quality contact formation, precise alignment of micrometer-scale patterns, and control of interfacial-adhesion/local-resistance. Here, a thermally controlled transfer printing technique that allows multiple patterned-graphene transfers at desired locations is presented. Using the thermal-expansion mismatch between the viscoelastic sacrificial layer and the elastic stamp, a "heating and cooling" process precisely positions patterned graphene layers on various substrates, including graphene prepatterns, hydrophilic surfaces, and superhydrophobic surfaces, with high transfer yields. A detailed theoretical analysis of underlying physics/mechanics of this approach is also described. The proposed transfer printing successfully integrates graphene-based stretchable sensors, actuators, light-emitting diodes, and other electronics in one platform, paving the way toward transparent and wearable multifunctional electronic systems.

1. Introduction

As transparent and wearable electronics are under spotlights, diverse nanoscale materials, such as carbon nanomaterials, ultrathin inorganic nano-ribbons/membranes, and nanowire composites, have been intensively studied.[1,2] Particularly among them, graphene has received significant attentions due to its uniquely beneficial properties including mechanical flexibility, optical transparency, high conductivity/carrier mobility, and thermal responsiveness.[3–5] Various individual graphene-based devices (e.g., transistors,[6–8] memory devices,[9] light-emitting diodes (LEDs),[10,11] optical[12] and mechanical[13,14] sensors, electrical[15] and thermal[16] actuators, and cell culture devices[17] have been demonstrated. The ultimate goal of this research trend is the integration of diverse graphene-based electronic/optoelectronic devices toward multifunctional all-graphene electronic systems, i.e., a well-organized array of graphene devices interconnected by graphene electrodes.[18,19] However, the photolithographical patterning and oxygen plasma etching of graphenes on preformed graphene passive/active components and/or other functional electronic materials/units are limited by several processing hurdles.[20–23] A viable route for the goal is to organize/integrate multiple stacks of patterned graphene device components by using the aligned transfer printing technique.[24,25]

High-quality graphene, which is synthesized on metal foils using the chemical vapor deposition,[26,27] is typically transferred

M. K. Choi, I. Park, D. C. Kim, E. Joh, J. Kim, M. Kim, C. Choi, J. Yang, K. W. Cho, Prof. T. Hyeon, Prof. D.-H. Kim
Center for Nanoparticle Research
Institute for Basic Science (IBS)
Seoul 151-742, Republic of Korea
E-mail: dkim98@snu.ac.kr

M. K. Choi, I. Park, D. C. Kim, E. Joh, J. Kim, M. Kim, C. Choi, J. Yang, K. W. Cho, Prof. T. Hyeon, Prof. D.-H. Kim
School of Chemical and Biological Engineering
and Institute of Chemical Processes
Seoul National University
Seoul 151-742, Republic of Korea

Dr. O. K. Park
Division of Bio-imaging
Korea Basic Science Institute
Chun-Cheon 200-701, Republic of Korea

J.-H. Hwang, Prof. J.-M. Nam
Department of Chemistry
Seoul National University
Seoul 151-742, Republic of Korea

Prof. J. H. Kim
School of Mechanical Engineering
Pusan National University
Busan 609-735, Republic of Korea
E-mail: kimjh@pusan.ac.kr

DOI: 10.1002/adfm.201502956

onto target substrates using thermal release tapes[28] or through scooping method with sacrificial polymer layers,[29–33] such as poly(methylmethacrylate) (PMMA),[30,31] polystyrene (PS),[32] and polyisobutylene (PIB).[33] These methods have been successfully applied in large-scale graphene transfer procedures.[27,28,34] Recently, novel direct transfer printing methods using electrochemical delamination[35] or static electricity[36] have been proposed and demonstrated significantly low sheet resistance and high-quality graphene surface by eliminating contaminations from organic/inorganic residues. Many challenges still exist, however, in multiple aligned transfer of graphene patterns and device components onto prepatterned ones. Transfer printing using the elastomeric polydimethylsiloxane (PDMS) stamp[37] has been successfully demonstrated to selectively pick up inorganic[38–41] and metal nanomembranes,[42] nanoparticles,[43] and carbon nanotubes[44] and position them on preregistered target locations. However, in spite of these advances, the multiple transfer of patterned graphene using elastomeric stamps on diverse substrates has remaining challenges to achieve high-quality interfaces, micrometer-range alignments, and high success rates (i.e., yields).

Here, a simple but effective aligned transfer printing process of patterned graphene device components is developed. Key advancements are in the use of designed thermal treatment sequences as well as viscoelastic sacrificial polymers with elastomeric stamps for the efficient patterned graphene transfer. The heating and cooling protocol results in the dramatic increase of the transfer yield (from ≈27% to ≈90%) in comparison with conventional procedures (method without thermal treatments). The proposed high-fidelity multiple transfer printing technique along with in-depth understanding of related materials and mechanics in processes and device designs enables the transparent and wearable all-graphene multifunctional electronic system.

2. Results and Discussion

A representative example of multifunctional integrated system based on wearable graphene electronic/optoelectronic devices fabricated through the thermally controlled transfer printing process is illustrated in **Figure 1**. The multi-stacked and stretchable graphene devices (sensors, actuators, and LEDs) are conformally laminated on the human skin and connected to a smart band that contains a controller, a power-supply module, and a wireless data transmission unit (Figure 1a). The ultrathin thickness of graphene circuits in addition to meandering device designs enables the high stretchability.[45,46] The portable, invisible, and multifunctional features of this wearable system enlist many applications. One application scenario in the personalized healthcare, for example, is as follows. Integrated sensors monitor bio-signals of the user (e.g., activity and/or tremor) in real time (Figure 1b). The collected information is wirelessly transmitted to the external smart devices (e.g., smartphone) through a Bluetooth module in the smart band (Figure 1a and Movie S1, Supporting Information). When acute, abnormal conditions are to be notified to the user, the quantum dot (QD) LEDs are turned on (Figure 1c). Electrical and thermal actuators (iontophoresis electrodes and heater) effectively induce feedback transdermal drug delivery and/or thermal physiotherapy (Figure 1d,e). The feedback actuation can be remotely controlled through a custom-made Android application (Movie S2, Supporting Information).

Figure 2a is a schematic diagram of the thermally controlled, aligned transfer printing process of graphene patterns. The insets are optical camera images of graphene layers at each step; note that the transparent graphene patterns are colorized for ease of viewing. First, non-patterned graphene monolayers are stacked on the graphene grown on the Cu foil using the conventional transfer method[26,27] to adjust the

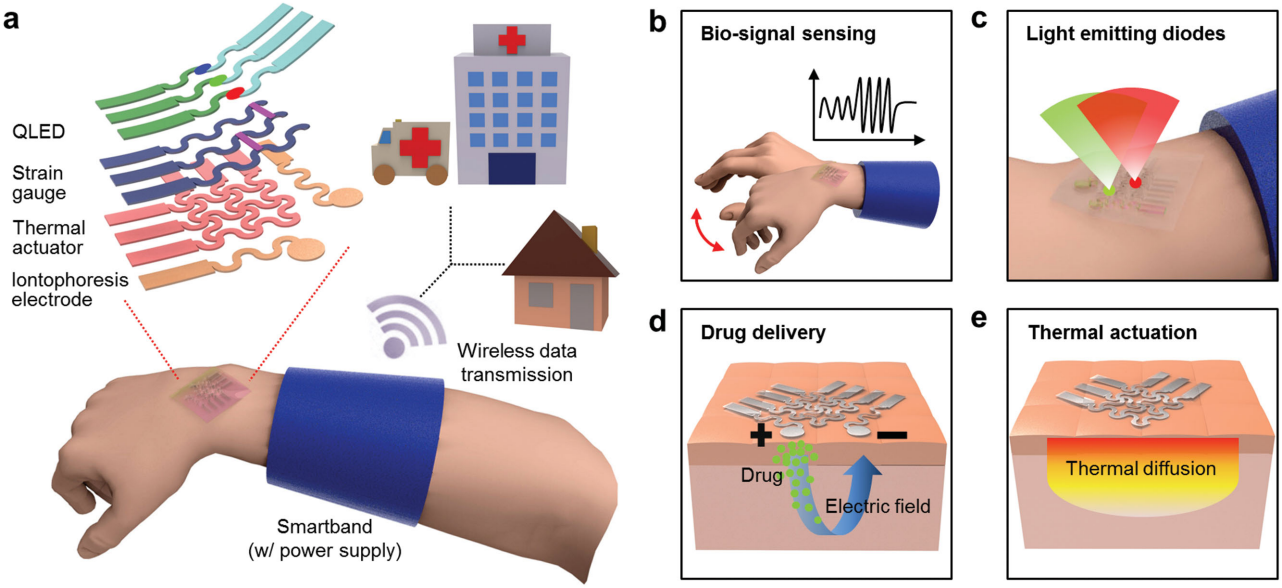

Figure 1. Schematic illustrations of the wearable and transparent graphene electronic/optoelectronic system. a) Exploded view of stacked graphene devices and system integration. Multiple functions of the integrated wearable system; b) sensing bio-signals, showing alarms through c) light-emitting diodes, d) transdermal drug delivery, and e) thermal therapy.

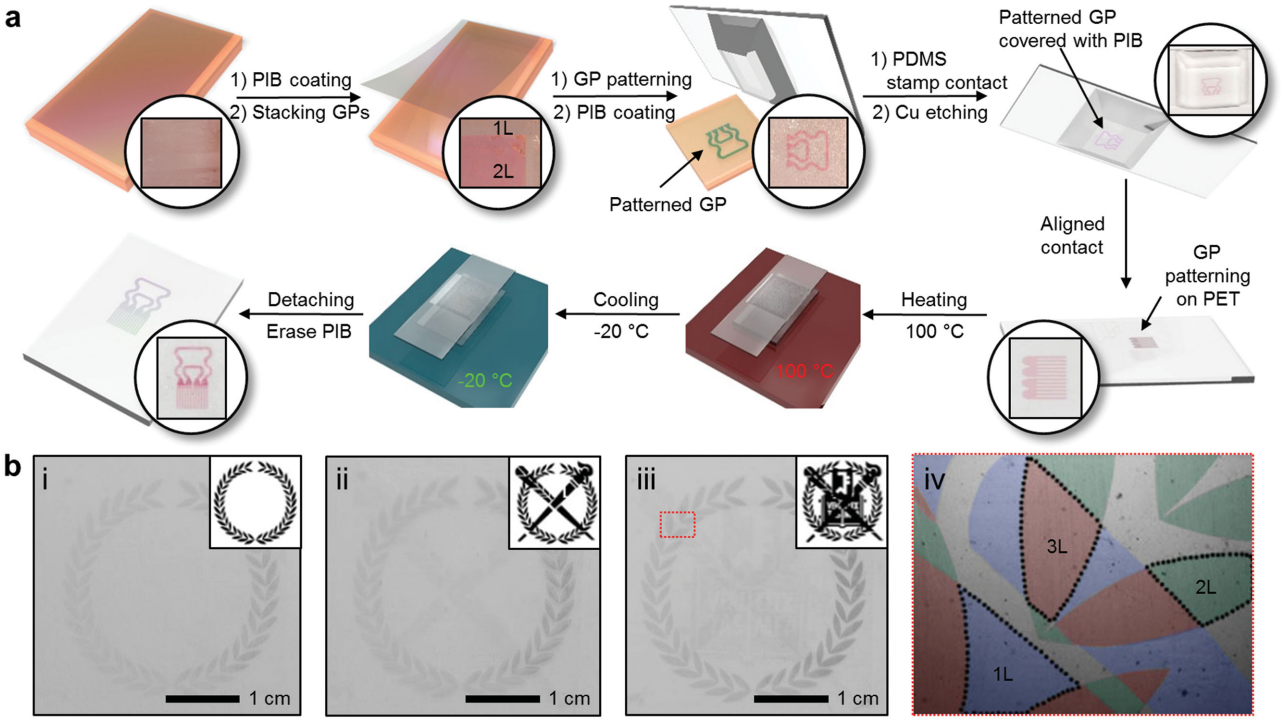

Figure 2. Thermally controlled transfer printing of the patterned graphene. a) Schematic illustration of the thermally controlled transfer printing process. b) Sequential optical images of the multiple and aligned transfer printing of graphene patterns (i–iii). The area enclosed by a red dotted box in frame (iii) is magnified in (iv). The image is colored to indicate the different number of patterned graphene layers.

resistance of the graphene layers.[16] The resulting resistance-controlled multi-stacked graphene is photolithographically patterned so that the desired features/designs are obtained. Then, the patterned graphene is coated with a viscoelastic sacrificial layer of PIB[33] and conformal contact is made with the PDMS stamp. $FeCl_3$ solution is used to chemically etch the Cu foil and releases the graphene/PDMS stamp. After the etching solution is washed away, the graphene-holding stamp is aligned to make a contact with the target substrates and/or prepatterned graphene layers (Figure S1, Supporting Information). To increase the interfacial adhesion, the contacted system (stamp/patterned-graphene/substrate) is heated to 100 °C. Subsequent cooling to –20 °C and returning to room temperature completes the transfer process. During the low-temperature stage, the thermal expansion coefficient mismatch between the PIB and PDMS focuses the mechanical stress at the edge of the PIB/PDMS interface, which enables easy separation of the PDMS stamp from the patterned-graphene on the substrate and thereby increases the transfer yield. After the transfer printing, the PIB sacrificial layer is removed using the decane solution. Figure 2b shows a representative example of the thermally controlled multiple transfer printing of graphene patterns (i–iii). Insets show the design of graphene patterns (university logo). The colorized image in Figure 2b frame iv is a magnified view of the red dotted box in frame iii, in which precise pattern overlaps without defects for resistance controls and high-quality graphene–graphene interfaces can be observed.

We statistically analyzed the influence of different thermal treatment sequences on the yield of transfer printing by using ≈400 patterned graphene samples. We used samples of an array of square patterns (size: 300 × 300 μm^2). **Figure 3**a summarizes the obtained transfer printing yields at various thermal treatment conditions. Representative raw data are shown in Figure S2 (Supporting Information). As demonstrated in the previous reports,[20,21,27,28,34] large-area graphene patterns/films are easily transferred on desired substrates because of the strong van der Waals force between graphene and receiving substrates. However, as the graphene pattern size decreases, which is necessary for high-density electronics and optoelectronics, the van der Waals force decreases dramatically.[47] Since the adhesion force between graphene and target substrates is smaller than that between PIB and PDMS at room temperature in particular, small graphene patterns are easily delaminated from the receiving substrates during the retrieval process of the PDMS stamp (Figure 3b,c).

The designed thermal treatment sequences overcome this problem. We compared representative optical microscope images of thermally treated graphene layers at different temperature sequences (see Figure 3c–e for transfer printing at room temperature, after heating, and after heating–cooling, respectively). To show the differences in each transfer printing process more clearly, images of the graphene samples were collected before the removal of the PIB. Due to thermal treatments, the transfer yield increases from 27% (no treatment) to 78% (heating only) and to 90.5% (heating–cooling). This thermally controlled transfer printing technique can be applied over the large area (size: 5 cm × 5 cm; Figure S3, Supporting Information, inset shows the magnified view) on an ultrathin PET substrate (thickness: ≈4.5 μm) of various surface properties

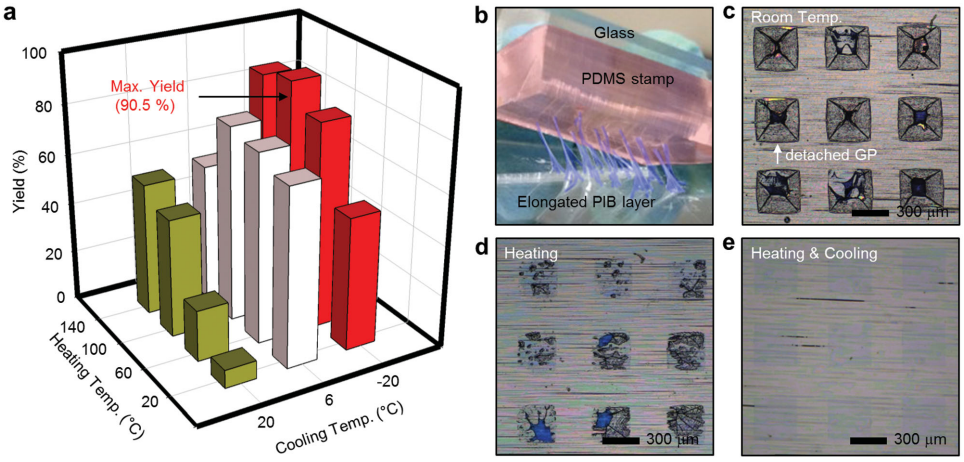

Figure 3. Experimental evaluation of "heating and cooling" sequences. a) Effects of different thermal treatment sequences on the transfer printing yield. b) Colorized optical camera image of the failed graphene transfer printing without the thermal treatment (at room temperature). Graphene layers transferred by using c) PIB at room temperature, d) after heating treatment, and e) after heating and cooling treatment.

(from hydrophilic to superhydrophobic surfaces; Figure S4, Supporting Information).

A detailed theoretical analysis of the mechanism behind the thermally controlled graphene transfer process was conducted, based on the experimental data shown in **Figure 4**. The PDMS, PIB, and glass substrate have different thermal expansion behaviors, as shown in Figure 4a. These differences in thermal expansion properties result in a thermal expansion mismatch, which causes a stress build-up between the layers in response to temperature changes. In addition, PIB exhibits quite large viscoelasticity (Figure 4a), which affects the amount of induced stress. The stress relaxation in PIB was measured at 20 °C (black dots), 60 °C (blue dots), and 100 °C (red dots), as shown in Figure 4b. From a theoretical perspective, the relaxation modulus can be described by a series of exponential decaying functions

$$G(t) = \sum_{i=1}^{4} w_i \exp\left[-\left(\frac{t}{\tau_i}\right)\right] \quad (1)$$

where $G(t)$ is the relaxation modulus at time, w_i is the weighting factor ($\sum_{i=1}^{4} w_i = 1$), and τ_i is the relaxation t time. If the viscosity follows the Arrhenius dependence on the temperature, the shift factor ψ is given by

$$\psi = \exp\left(\frac{H}{R}\left(\frac{1}{T_R} - \frac{1}{T}\right)\right) \quad (2)$$

where H is the activation enthalpy for stress relaxation, R is the universal gas constant, T_R is the reference temperature (100 °C in this analysis), and T is the current temperature. The reduced time ξ is defined by the shift factor as

$$\xi = \int_0^t \psi(t')\,dt' = \int_0^t \exp\left(\frac{H}{R}\left(\frac{1}{T_R} - \frac{1}{T(t')}\right)\right)dt'. \quad (3)$$

The stress relaxation at different temperatures can be represented by replacing t with ξ in Equation (1). The model parameters are obtained from the stress relaxation data. Figure 4b shows the fitted results for the data obtained at 20 °C (black line), 60 °C (blue line), and 100 °C (red line), along with a prediction for –20 °C (dark green line). At 100 °C, 90% of the applied stress was found to be relaxed after 1200 s, whereas only 20% is expected to be relaxed at –20 °C. The thermally controlled graphene transfer process utilizes this difference in the stress relaxation during the thermal cycle.

The role of the thermal cycle in the development of the thermal stress at the edge of the PIB/PDMS interface, which is a critical factor for easy separation of the PDMS stamp from the patterned-graphene/substrate, was examined by using a thermo-mechanical finite element simulation (Figure 4c,d). The PDMS/PIB/PET substrate structure was modeled by 2D plane strain elements. Because the analysis was focused on the PDMS/PIB interface, the graphene between the PIB and PET substrate was ignored. Linear elasticity and linear thermal expansion were assumed for the PDMS and the PET substrate, whereas the viscoelasticity model was used for the PIB (Figure 4c). To determine the effect of the viscoelasticity on the thermal stress, the results for the elastic PIB were also calculated (Figure 4d). As the interfacial stress is strongly affected by modulus and thickness, we experimentally obtained modulus (Table S1, Supporting Information) and thickness (Figure 4a) of PIB and PDMS layers at various temperatures. The initial temperature of the finite element model was set to 20 °C. As the temperature increases from 20 °C to 100 °C (heating), the thermal strain mismatch between the layers instantly generates shear stresses, as seen on the left of Figure 4c. After a 10-min period at a fixed temperature of 100 °C, the majority of the stress was relaxed (Figure 4c, middle), as expected from Figure 4b. When the sample was cooled to –20 °C, a large shear stress was developed at the PDMS/PIB interface (Figure 4c, bottom), promoting easy separation of the materials during the transfer process. The shear stress developed at the PIB/PET interface does not lead to separation due to the strong adhesion between PIB and substrate according to the experimental results. Note that, if PIB is elastic, holding the temperature at 100 °C does not cause the developed stress to relax (Figure 4d, top and middle) and cooling to –20 °C leaves only a small amount of shear stress (Figure 4d, bottom).

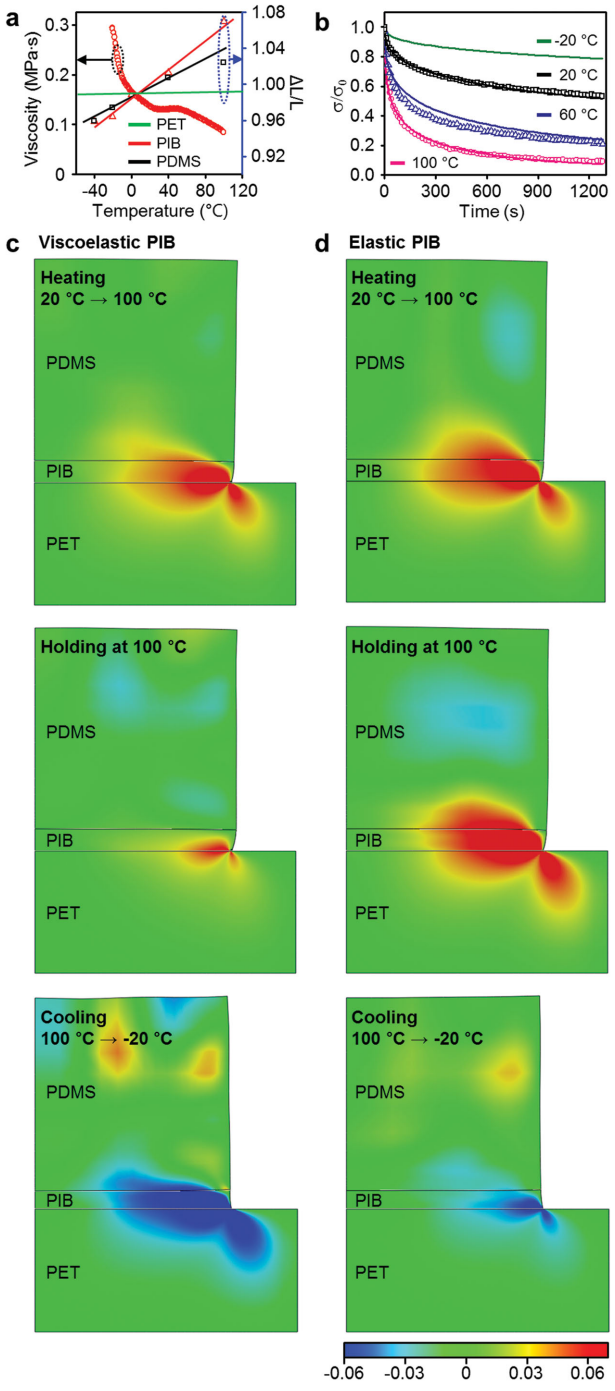

Figure 4. Simulation of the elastic and viscoelastic behaviors of PDMS, PIB, and PET layers during the thermal treatment. a) Temperature dependence of PIB viscosity and thermal expansion behavior of PDMS, PIB, and PET. b) Stress relaxation of PIB at various temperatures (dot: measured data, line: model prediction). c,d) FEM-predicted shear stress in PDMS, PIB, and PET substrate after heating from 20 °C to 100 °C, holding for 10 min, and cooling to −20 °C. The c) viscoelasticity and d) linear elasticity models were used for PIB.

Furthermore, we directly compared the effect of sequential thermal treatments in the interfacial energy of PIB/PDMS and PIB/PET using a peel test. After the heating and cooling thermal treatment, the relative adhesion force of PIB/PDMS is ≈14% decreased and that of PIB/PET is ≈200% increased. The detailed results are shown in Figure S5 (Supporting Information).

To validate the quality of graphene patterns/stacks fabricated through the thermally controlled multiple transfer printing processes, we examined their optical and electrical properties through various material characterization methods. Imaging using atomic force microscopy (AFM) confirms the integrity and quality of the transferred graphene surface (**Figure 5**a). The AFM phase image presents the pure graphene layer without organic residues (Figure 5b). Raman spectroscopy analysis (Figure 5c) shows the high intensity at the typical G-band for the graphene monolayer with the minimal one at the defect band. The 2D Raman mapping analysis (area: 280 μm × 220 μm) confirms the uniform and high-quality surface of graphene prepared by thermally controlled transfer printing method (Figure S6, Supporting Information).

The thermally controlled transfer printing technique readily forms various resistance/transparency distributions (Figure 5d–g). A graphene pattern with different electrical and optical properties can be achieved using the proposed transfer printing technique (see Figure 5e–g for its optical image, sheet resistance, and transparency, respectively). Figure 5d summarizes various sheet resistances and transparencies of multi-stacked graphene layers. By stacking Au-doped graphene layers and/or hybridizing with Ag nanowires, the graphene sheet resistance can be controlled from ≈60 to ≈1500 Ω $\square^{-1}$, which corresponds to ≈80% to ≈95% transparency. The minimum resolution of the thermally controlled transfer printing was 5 μm in our experiment. 5 μm grid patterns, spaced with 25, 50, 100, and 200 μm, were successfully transfer printed (Figure S7, Supporting Information). This patterned graphene transfer printing can be applied to various substrates including the PDMS substrate with various modulus (from 20 kPa to 2 MPa; Figure 5h). Figure 5i shows the variety of examples of the multi-stacked aligned graphene patterns (i: crane, ii: line and space, and iii: partially overlapped square patterns).

This thermally controlled transfer printing technique can be applied to various device fabrications. Graphene-based sensors and actuators (temperature sensor, strain gauge, and thermal actuator) on a flexible PET substrate, for example, are shown in **Figure 6**. The resistance of the fabricated temperature sensor varies linearly at different temperatures (Figure 6a,b), with a sensitivity of ≈30 Ω $°C^{-1}$. The gauge factor of the graphene strain gauge is found to be ≈2.1 (Figure 6c,d). The resistance of the sensing unit is designed ≈50 times greater than that of the interconnection. Therefore, the resistance changes of sensors induced by variations in the temperature and external strain are significantly higher than those of the interconnection, which maximizes the sensitivity. Figure 6e,f show images of graphene heater and corresponding thermal characterization data (at an applied voltage of ≈10 V). Thermal images are obtained using a commercial infrared camera (FLIR i5, FLIR system, USA). The regions i, ii, and iii are composed of the rectangular graphene pattern of ≈1400 (single layer), ≈700 (double layer), and ≈300 Ω $\square^{-1}$ (triple layer), respectively. The multiple aligned transfer printing defines regions of different resistances. The temperature versus voltage curves for regions of i, ii, and

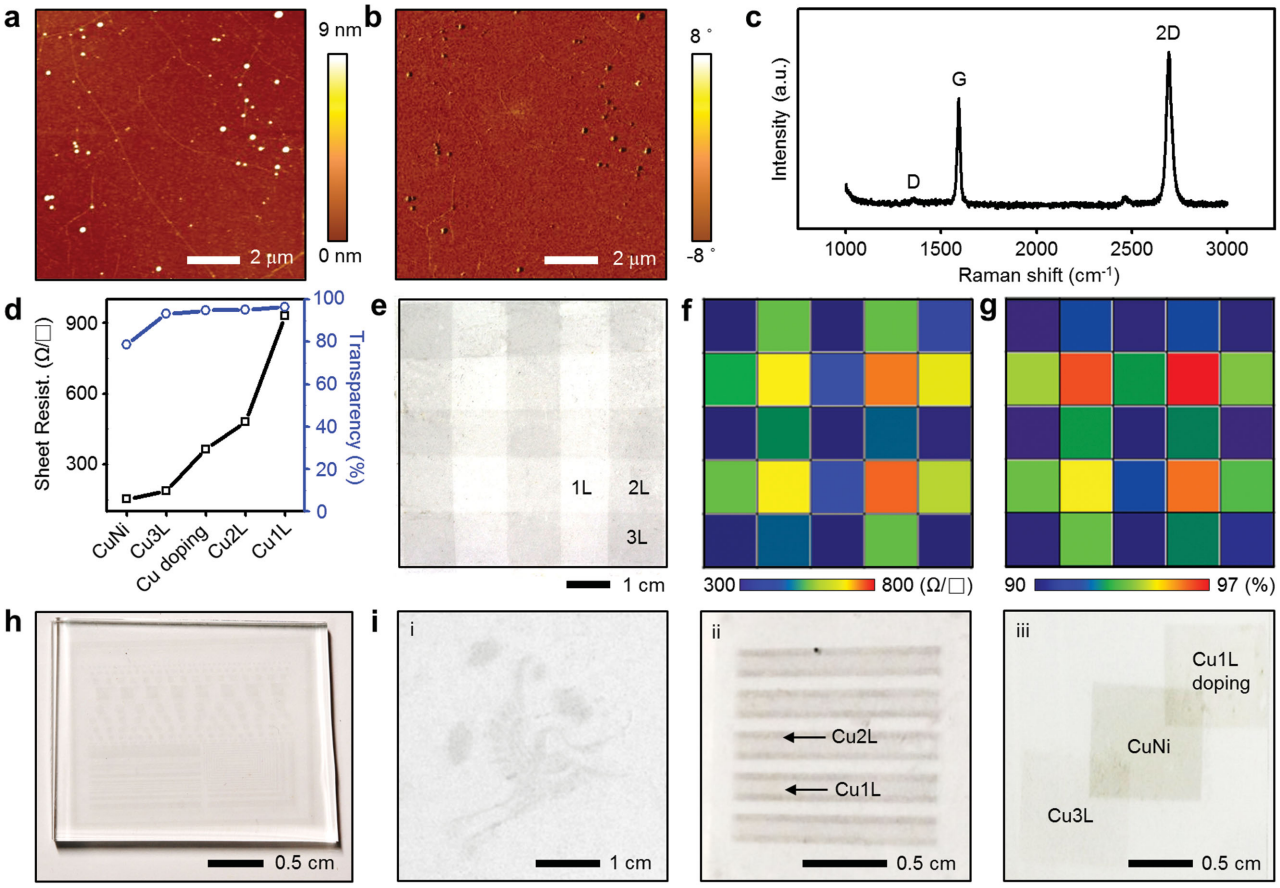

Figure 5. Electrical and optical properties of transferred graphene patterns. Atomic force microscopy: a) height image and b) phase image of graphene patterns transferred onto 300 nm thick SiO_2 substrate. c) Raman spectrum from thermally controlled transfer-printed graphene layer. d) Sheet resistance and transparency of various resistance-controlled graphene layers. e) Optical image of a stacked graphene pattern. f) Areal distribution of sheet resistance and g) transparency. h) Optical image of the transferred graphene pattern on the PDMS substrate. i) Various multi-stacked graphene patterns.

iii provide more quantitative data on the thermal actuation (Figure 6g). The multiple graphene stack shows the lower resistance and higher joule heating response. The rapid joule heating of graphene resistors, particularly in design iii, effectively controls the local temperature.

Integration of individual devices together with a custom-made smart band enables a transparent and wearable sensor and actuator with the wireless data transmission and control. The wearable system is designed to be conformally laminated on the human skin, which maximizes the sensor sensitivity and feedback actuation efficiency. The resulting array fabricated via the thermally controlled transfer printing is shown in **Figure 7**a,b (inset of Figure 7b shows the magnified view). The graphene devices are connected by graphene electrodes and encapsulated by transparent, ultrathin (< ≈1 μm) epoxy layers (SU8-2, MicroChem, USA). The graphene devices are located on the neutral mechanical plane to dissipate the bending-induced strain. The intrinsic softness of the graphene enhances the mechanical reliability of the system further.[48] The strain gauge in the integrated system successfully monitors human physical activity or tremor by characterizing joint movements. Figure 7c shows the cyclic fatigue test result, which exhibits no performance changes over 1000 times of bending (bending radius ≈500 μm). The ultrathin (overall thickness < ≈2 μm) and stretchable design helps to maintain the robust contact between devices and soft human skin without delamination and thereby the signal to noise ratio is relatively high. The graphene wearable system is connected to the smart-band,[49] which includes the power supply, control, and wireless communication module (Figure 7d,e and Figure S8, Supporting Information for representative wireless experimental setup image, schematic circuit diagram of the smart band, and its image, respectively). The tremor signals measured by the strain gauge,[43] for instance, are wirelessly transmitted to the external electronic devices (e.g., smartphone and/or tablet) via Bluetooth. Figure 7f shows the transmitted signals to the external computer after the noise filtering (see Movie S1, Supporting Information).

The information display is another important component in the electronic/optoelectronic system to provide signals and/or alarms to the user. The graphene electrode can be used for wearable quantum dot LEDs (QLEDs).[47] An emergency alarm, for example, can be displayed to the user through the skin-mounted QLEDs. QLEDs have many advantages, such

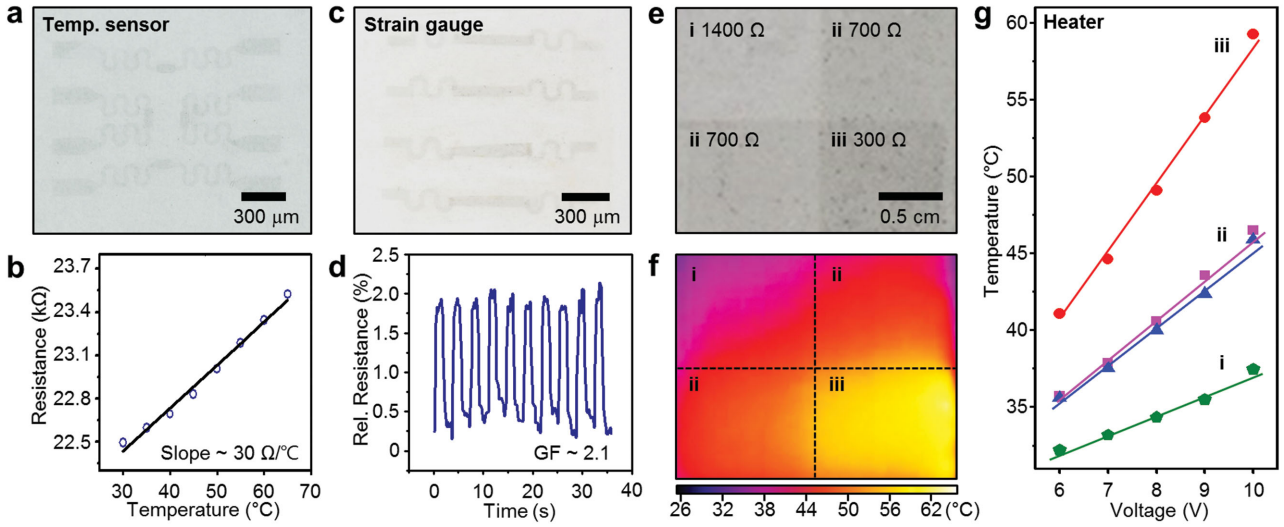

Figure 6. Characterization of graphene-based sensors and actuators. a) Optical image and b) calibration curve (sensitivity: ≈30 Ω °C^{-1}) of the graphene temperature sensor. c) Optical image and d) characteristic curve (gauge factor ≈2.1) of the strain gauge. Optical image of e) graphene heaters, f) corresponding IR camera image at 10 V applied bias, and g) thermal response characterization of each region.

as the color purity, air/water stability, ultrathinness, and cost-effectiveness, and become an emerging candidate for the flexible and stretchable display. Despite recent advances in QLED technologies, accomplishing deformable QLEDs is a daunting goal due to poor mechanical deformability of ITO anodes. By virtue of the transparency and flexibility of the graphene electrodes, wearable QLEDs could be fabricated (**Figure 8**). The exploded illustration (Figure 8a) provides the layer information and inset images show wearable QLEDs on the human arm. The QLEDs are stacked on top of the wearable sensors and actuators. The semitransparent Li/Al alloy cathodes are shown, while the graphene anodes are invisible. Figure 8b shows the band structure of the QLED including the anode and cathode, hole- and electron-transporting layer, and light-emitting layer. Current density and brightness at various applied voltages (*J*–*V*–*L* performance) and electroluminescence efficiency (EQE) of the QLEDs are presented in Figure 8c,d, respectively. The wearable QLEDs are operated with a commercial microbattery (Figure S8, Supporting Information) by virtue of their low required power consumption. Bending deformations up to 180° do not change the QLED performance (Figure 8e).

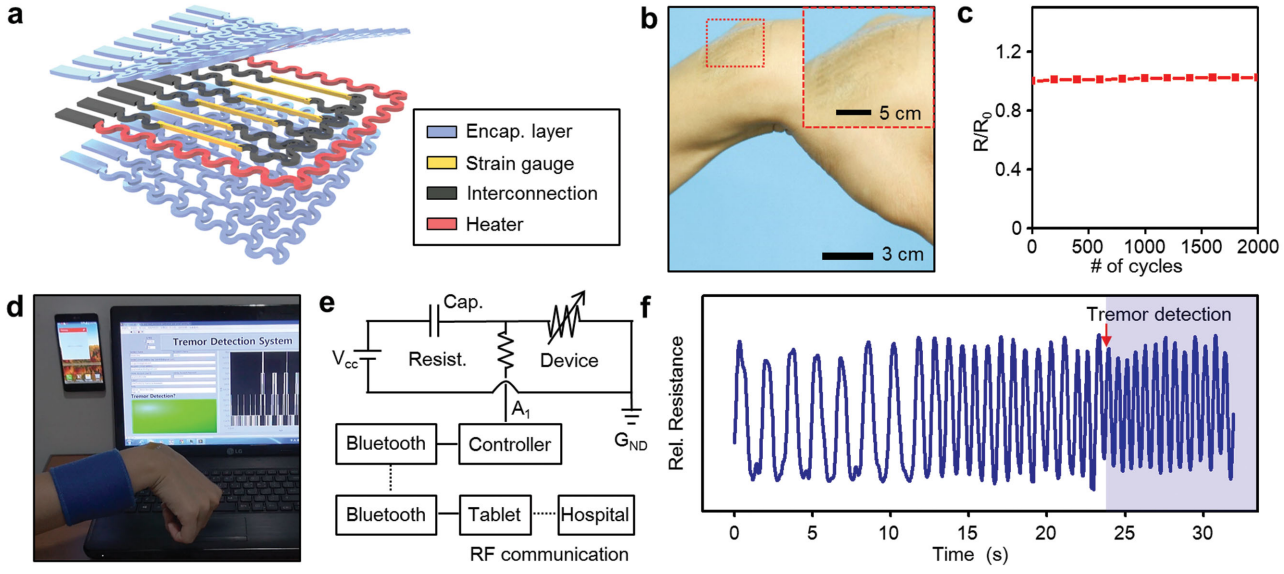

Figure 7. Integrated wearable sensors and actuators. a) Exploded illustration of the wearable sensors and actuators. b) Optical image of the graphene electronic system conformally laminated on the wrist, which corresponds to Figure 7a. Inset shows the magnified view. c) Relative resistance change during the cyclic bending test. d) Image of the wireless tremor detection system and e) its schematic circuit diagram. f) Wirelessly transmitted motion and tremor signals after the noise filtering.

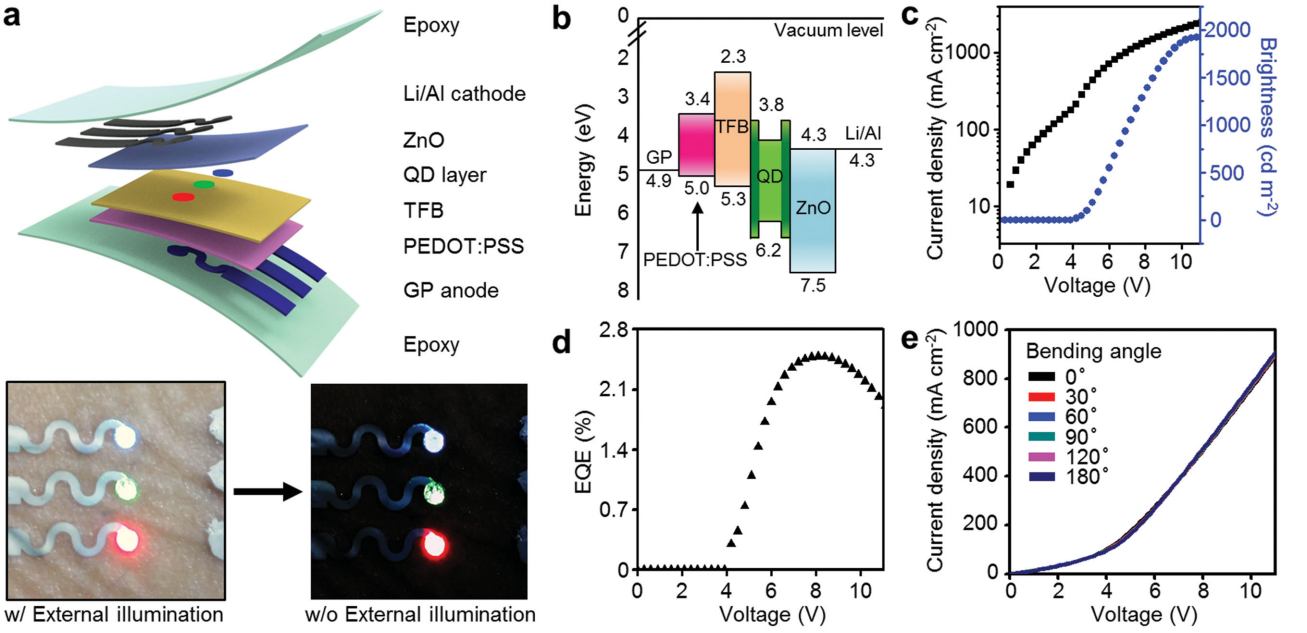

Figure 8. Wearable QLED with the graphene anode. a) Exploded illustration of the wearable QLED. The insets at the bottom show corresponding images of the QLED laminated on the human arm with (left) and without (right) the external illumination. b) Energy band diagram of the QLED. c) *J–V–L* characteristics and d) external quantum efficiency of the wearable QLED. e) Stable *J–V* characteristics of the QLED at various bending angles (from 0° to 180°).

Feedback actuations in relation to the sensing are crucial to complete the loop of sensing and actuation.[43] **Figure 9** shows the representative example, a wirelessly controlled feedback actuation for the thermal therapy[50] (by heaters) and the transdermal drug delivery[43,51] (by iontophoresis electrodes) in response to the measured data from integrated sensors (see Figure 9a and Movie S2, Supporting Information). Thermal energy diffusion from graphene heaters to dermal and vascular tissues near the wrist is shown in Figure 9b (infrared and optical camera image in the left and right frame). Thermal therapy is a widely used physical treatment.[48] The conformal lamination of the heater on the skin maximizes the heat transfer and

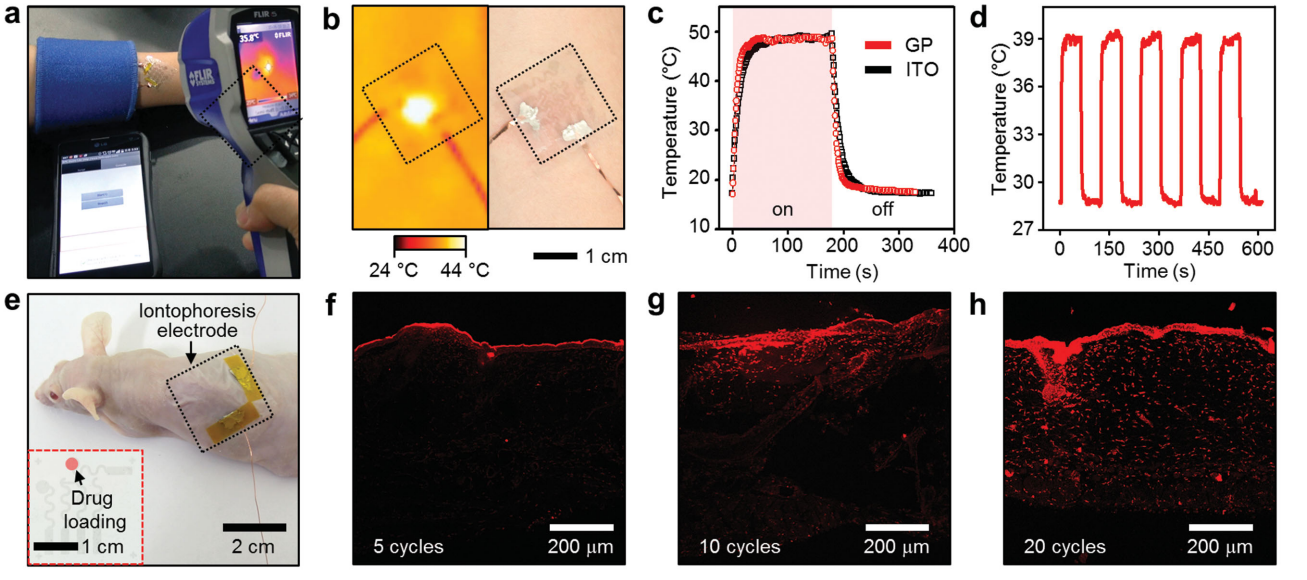

Figure 9. Feedback thermal and electrical actuators. a) Wirelessly controlled graphene thermal actuator using a custom-made smartphone application. b) IR (left) and optical (right) image of the graphene heater laminated on the skin. c) Comparison of thermal responses of transparent heaters made of graphene (GP) and indium-tin-oxide (ITO). d) Cyclic thermal stimulations. e) Image of transdermal drug delivery on the mouse skin using graphene iontophoresis electrodes. Inset shows the drug-loaded iontophoresis electrodes. f–h) Cross-sectional confocal microscope images showing transdermal drug delivery of doxorubicin (red) through the mouse skin. The penetration depth is proportional to the number of electrical stimulation.

physiotherapy efficiency. Note that the time-dependent thermal actuation properties of the graphene heater is similar with that of devices based on other transparent electrodes, such as an indium-tin-oxide (Figure 9c). Figure 9d shows repetitive on–off cycles of the heater (1 min period), presenting the stable and fast heating property. Another feedback actuation, transdermal drug delivery, is performed by using the local electric field formed by iontophoresis electrodes. Figure 9e shows the laminated iontophoresis electrodes on the skin of a nude mouse. Polar drugs (doxorubicin, Aldrich, USA) loaded on graphene electrodes are delivered through the skin and into the bloodstream by the applied electric field without any pain. The penetration depth can be easily tuned by controlling the number of stimuli. The confocal image shows that the penetration depth of the drug is proportional to the number of applied iontophoresis stimuli (Figure 9f–h).

3. Conclusion

In summary, we report a thermally controlled transfer printing technique for the integration of patterned graphene devices. The designed "heating and cooling" thermal treatment process transfers patterned graphene layers intact on various substrates. Furthermore, aligned transfer printing allows the accurate integration of stretchable graphene electronic/optoelectronic devices in an ultrathin wearable platform. The resulting multifunctional wearable system is conformally laminated on the human skin to successfully carry out physiological sensing, wireless data transmission, signal display, thermal physiotherapy, and transdermal drug delivery, together with a custom-made smart band. These advances would provide new opportunities for all-graphene integrated systems.

4. Experimental section

"*Heating and Cooling*" *Transfer Printing of Patterned Graphene*: Monolayer graphene was synthesized using the chemical vapor deposition procedure.[21] The graphene film was doped with the Au salt and stacked on another graphene film on a Cu foil in order to control the conductivity (details are in the Supporting Information). After adjusting the graphene resistance, the stacked graphene layers on the Cu foil were patterned using photolithography and O_2 plasma etching. The patterned graphene was spin coated with a PIB solution (30 mg mL^{-1} in n-decane solvent, Aldrich, USA), and annealed at 100 °C for 1 min so as to vaporize the decane (Samchun Chemical, Republic of Korea). A 10 mm thick PDMS elastomer stamp (Sylgard 184, Dow Corning, USA) was then put into conformal contact with the PIB layer. The Cu/graphene/PIB/PDMS structure was immersed in the $FeCl_3$ solution in order to dissolve the Cu foil, and was then washed with deionized water and dried at room temperature. Then, the graphene/PIB/PDMS assembly was aligned on the target transfer printing location. To increase the interfacial adhesion, the sample was heated on a hotplate at 100 °C for 10 min, followed by cooling at –20 °C for 30 min. In the final stage of the transfer printing process, the PDMS stamp was gently detached from the substrate and the PIB layer was removed using pure decane. A Raman spectrum of graphene film was analyzed using T64000 (Horiba, Japan) at NCIRF and the AFM measurement was performed in the tapping mode (Dimension iCON, Bruker, Germany).

Other Materials and Methods: Other materials and methods are available in the Supporting Information.

Supporting Information

Supporting Information is available from the Wiley Online Library or from the author.

Acknowledgements

C.M.K., P.I., and K.D.C. contributed equally to this work. This research was supported by IBS-R006-D1. This work was supported by a Seoul National University Research Grant. Balb/c nude mice (age: 6 weeks) were obtained from the Experimental Animal Center, Chuncheon Center, Korea Basic Science Institute (KBSI), Chuncheon, South Korea. All animal procedures were in accordance with the Guide for the Care and Use of Laboratory Animals issued by the Laboratory Animal Resources Commission of KBSI. The Institutional Animal Care and Use Committee at the KBSI (KBSI-AEC1409) reviewed and approved this study.

Received: July 17, 2015
Revised: August 27, 2015
Published online: October 15, 2015

[1] D.-H. Kim, N. Lu, R. Ghaffari, J. A. Rogers, *NPG Asia Mater.* **2012**, *4*, e15.
[2] T. Sekitani, H. Nakajima, H. Maeda, T. Fukushima, T. Aida, K. Hata, T. Someya, *Nat. Mater.* **2009**, *8*, 494.
[3] K. S. Novoselov, V. I. Fal'ko, L. Colombo, P. R. Gellert, M. G. Schwab, K. Kim, *Nature* **2012**, *490*, 192.
[4] Q. Bao, K. P. Loh, *ACS Nano* **2012**, *6*, 3677.
[5] D. H. Lee, J. Yi, J. M. Lee, S. J. Lee, Y.-J. Doh, H. Y. Jeong, Z. Lee, U. Paik, J. A. Rogers, W. I. Park, *ACS Nano* **2013**, *7*, 301.
[6] W. H. Lee, J. Park, Y. Kim, K. S. Kim, B. H. Hong, K. Cho, *Adv. Mater.* **2011**, *23*, 3460.
[7] T. Q. Trung, N. T. Tien, D. Kim, M. Jang, O. J. Yoon, N.-E. Lee, *Adv. Funct. Mater.* **2014**, *24*, 117.
[8] T. Q. Trung, S. Ramasundaram, S. W. Hong, N.-E. Lee, *Adv. Funct. Mater.* **2014**, *24*, 3438.
[9] X. Wang, W. Xie, J.-B. Xu, *Adv. Mater.* **2014**, *26*, 5496.
[10] J.-T. Seo, J. Han, T. Lim, K.-H. Lee, J. Hwang, H. Yang, S. Ju, *ACS Nano* **2014**, *8*, 12476.
[11] T.-H. Han, Y. Lee, M.-R. Choi, S.-H. Woo, S.-H. Bae, B. H. Hong, J.-H. Ahn, T.-W. Lee, *Nat. Photonics* **2012**, *6*, 105.
[12] F. Xia, T. Mueller, Y.-M. Lin, A. Valdes-Garcia, P. Avouris, *Nat. Nanotechnol.* **2009**, *4*, 839.
[13] S. H. Bae, Y. Lee, B. K. Sharma, H. J. Lee, J. H. Kim, J. H. Ahn, *Carbon* **2013**, *51*, 236.
[14] Y. Wang, L. Wang, T. Yang, X. Li, X. Zang, M. Zhu, K. Wang, D. Wu, H. Zhu, *Adv. Funct. Mater.* **2014**, *24*, 4666.
[15] S. Lim, D. Son, J. Kim, Y. B. Lee, J.-K. Song, S. Choi, D. J. Lee, J. H. Kim, M. Lee, T. Hyeon, D.-H. Kim, *Adv. Funct. Mater.* **2015**, *25*, 375.
[16] J. Kang, H. Kim, K. S. Kim, S.-K. Lee, S. Bae, J.-H. Ahn, Y.-J. Kim, J.-B. Choi, B. H. Hong, *Nano Lett.* **2011**, *11*, 5154.
[17] S. J. Kim, H. R. Cho, K. W. Cho, S. Qiao, J. S. Rhim, M. Soh, T. Kim, M. K. Choi, C. Choi, I. Park, N. S. Hwang, T. Hyeon, S. H. Choi, N. Lu, D.-H. Kim, *ACS Nano* **2015**, *9*, 2677.
[18] F. Withers, T. H. Bointon, M. F. Craciun, S. Russo, *ACS Nano* **2013**, *7*, 5052.
[19] S. Lee, K. Lee, C.-H. Liu, G. S. Kulkarni, Z. Zhong, *Nat. Commun.* **2012**, *3*, 1018.
[20] D.-Y. Wang, I.-S. Huang, P.-H. Ho, S.-S. Li, Y.-C. Yeh, D.-W. Wang, W.-L. Chen, Y.-Y. Lee, Y.-M. Chang, C.-C. Chen, C.-T. Liang, C.-W. Chen, *Adv. Mater.* **2013**, *25*, 4521.

[21] J. Kang, S. Hwang, J. H. Kim, M. H. Kim, J. Ryu, S. J. Seo, B. H. Hong, M. K. Kim, J.-B. Choi, *ACS Nano* **2012**, *6*, 5360.
[22] W. Jung, D. Kim, M. Lee, S. Kim, J.-H. Kim, C.-S. Han, *Adv. Mater.* **2014**, *26*, 6394.
[23] H. H. Kim, Y. Chung, E. Lee, S. K. Lee, K. Cho, *Adv. Mater.* **2014**, *26*, 3213.
[24] S. J. Kang, B. Kim, K. S. Kim, Y. Zhao, Z. Chen, G. H. Lee, J. Hone, P. Kim, C. Nuckolls, *Adv. Mater.* **2011**, *23*, 3531.
[25] A. Carlson, A. M. Bowen, Y. Huang, R. G. Nuzzo, J. A. Rogers, *Adv. Mater.* **2012**, *24*, 5284.
[26] X. Li, W. Cai, J. An, S. Kim, J. Nah, D. Yang, R. Piner, A. Velamakanni, I. Jung, E. Tutuc, S. K. Banerjee, L. Colombo, R. S. Ruoff, *Science* **2009**, *324*, 1312.
[27] K. S. Kim, Y. Zhao, H. Jang, S. Y. Lee, J. M. Kim, K. S. Kim, J.-H. Ahn, P. Kim, J.-Y. Choi, B. H. Hong, *Nature* **2009**, *457*, 706.
[28] S. Bae, H. Kim, Y. Lee, X. Xu, J.-S. Park, Y. Zheng, J. Balakrishnan, T. Lei, H. R. Kim, Y. I. Song, Y.-J. Kim, K. S. Kim, B. Ozyilmaz, J.-H. Ahn, B. H. Hong, S. Iijima, *Nat. Nanotechnol.* **2010**, *5*, 574.
[29] S. K. Lee, J. W. Yang, H. H. Kim, S. B. Jo, B. Kang, H. Bong, H. C. Lee, G. Lee, K. S. Kim, K. Cho, *ACS Nano* **2014**, *8*, 7968.
[30] J. W. Suk, A. Kitt, C. W. Magnuson, Y. Hao, S. Ahmed, J. An, A. K. Swan, B. B. Goldberg, R. S. Ruoff, *ACS Nano* **2011**, *5*, 6916.
[31] A. Reina, X. Jia, J. Ho, D. Nezich, H. Son, V. Bulovic, M. S. Dresselhaus, J. Kong, *Nano Lett.* **2009**, *9*, 30.
[32] E. H. Lock, M. Baraket, M. Laskoski, S. P. Mulvaney, W. K. Lee, P. E. Sheehan, D. R. Hines, J. T. Robinson, J. Tosado, M. S. Fuhrer, S. C. Hernandez, S. G. Walton, *Nano Lett.* **2012**, *12*, 102.
[33] J. Song, F.-Y. Kam, R.-Q. Png, W.-L. Seah, J.-M. Zhuo, G.-K. Lim, P. K. H. Ho, L.-L. Chua, *Nat. Nanotechnol.* **2013**, *8*, 356.
[34] L. Gao, G.-X. Ni, Y. Liu, B. Liu, A. H. C. Neto, K. P. Loh, *Nature* **2014**, *505*, 190.
[35] X. Wang, L. Tao, Y. Hao, Z. Liu, H. Chou, I. Kholmanov, S. Chen, C. Tan, N. Jayant, Q. Yu, D. Akinwande, R. S. Ruoff, *Small* **2014**, *10*, 694.
[36] W. Jung, D. Kim, M. Lee, S. Kim, J.-H. Kim, C.-S. Han, *Adv. Mater.* **2014**, *26*, 6394.
[37] A. Carlson, A. M. Bowen, Y. Huang, R. G. Nuzzo, J. A. Rogers, *Adv. Mater.* **2012**, *24*, 5284.
[38] J. Kim, M. Lee, H. J. Shim, R. Ghaffari, H. R. Cho, D. Son, Y. H. Jung, M. Soh, C. Choi, S. Jung, K. Chu, D. Jeon, S.-T. Lee, J. H. Kim, S. H. Choi, T. Hyeon, D.-H. Kim, *Nat. Commun.* **2014**, *5*, 11.
[39] H. Ko, K. Takei, R. Kapadia, S. Chuang, H. Fang, P. W. Leu, K. Ganapathi, E. Plis, H. S. Kim, S.-Y. Chen, M. Madsen, A. C. Ford, Y.-L. Chueh, S. Krishna, S. Salahuddin, A. Javey, *Nature* **2010**, *468*, 286.
[40] S. Yang, E. Ng, N. Lu, *Extreme Mech. Lett.***2015**, *2*, 37.
[41] D. Chanda, K. Shigeta, S. Gupta, T. Cain, A. Carlson, A. Mihi, A. J. Baca, G. R. Bogart, P. Braun, J. A. Rogers, *Nat. Nanotechnol.* **2011**, *6*, 402.
[42] Y.-L. Loo, R. L. Willett, K. W. Baldwin, J. A. Rogers, *J. Am. Chem. Soc.* **2002**, *124*, 7654.
[43] D. Son, J. Lee, S. Qiao, R. Ghaffari, J. Kim, J. E. Lee, C. Song, S. J. Kim, D. J. Lee, S. W. Jun, S. Yang, M. Park, J. Shin, K. Do, M. Lee, K. Kang, C. S. Hwang, N. Lu, T. Hyeon, D.-H. Kim, *Nat. Nanotechnol.* **2014**, *9*, 397.
[44] S. J. Kang, C. Kocabas, T. Ozel, M. Shim, N. Pimparkar, M. A. Alam, S. V. Rotkin, J. A. Rogers, *Nat. Nanotechnol.* **2007**, *2*, 230.
[45] M. Kaltenbrunner, T. Sekitani, J. Reeder, T. Yokota, K. Kuribara, T. Tokuhara, M. Drack, R. Schwödiauer, I. Graz, S. Bauer-Gogonea, S. Bauer, T. Someya, *Nature* **2013**, *499*, 458.
[46] D. P. J. Cotton, I. M. Graz, S. P. Lacour, *Sens. J. IEEE* **2009**, *9*, 2008.
[47] M. K. Choi, J. Yang, K. Kang, D. C. Kim, C. Choi, C. Park, S. J. Kim, S. I. Chae, T.-H. Kim, J. H. Kim, T. Hyeon, D.-H. Kim, *Nat. Commun.* **2015**, *6*, 7149.
[48] Y. Wang, R. Yang, Z. Shi, L. Zhang, D. Shi, E. Wang, G. Zhang, *ACS Nano* **2011**, *5*, 3645.
[49] M. K. Choi, O. K. Park, C. Choi, S. Qiao, R. Ghaffari, J. Kim, D. J. Lee, M. Kim, W. Hyun, S. J. Kim, H. J. Hwang, S.-H. Kwon, T. Hyeon, N. Lu, D.-H. Kim, *Adv. Healthcare Mater.* DOI:10.1002/adhm.201500285.
[50] S. Choi, J. Park, W. Hyun, J. Kim, J. Kim, Y. B. Lee, C. Song, H. J. Hwang, J. H. Kim, T. Hyeon, D.-H. Kim, *ACS Nano* **2015**, *9*, 6626.
[51] M. R. Prausnitz, R. Langer, *Nat. Biotechnol.* **2008**, *26*, 1261.